

Low temperature carbon co-implantation in silicon: Defects suppression and diffusion modeling

Cite as: J. Appl. Phys. 129, 195706 (2021); doi: 10.1063/5.0049782

Submitted: 9 March 2021 · Accepted: 4 May 2021 ·

Published Online: 20 May 2021



P. Dumas,^{1,2,a)} P.-L. Julliard,¹ J. Borrel,¹ S. Duguay,² F. Hilario,¹ F. Deprat,¹ V. Lu,³ W. Zhao,³ W. Zou,³ E. Arevalo,³ and D. Blavette²

AFFILIATIONS

¹STMicroelectronics, 850 Rue Jean Monnet, 38926 Crolles Cedex, France

²Université de Rouen, GPM, UMR CNRS 6634 BP 12, Avenue de l'Université, 76801 Saint-Étienne-du-Rouvray, France

³Applied Materials Gloucester, 35 Dory Road, Gloucester, Massachusetts 01930, USA

^{a)}Author to whom correspondence should be addressed: paul.dumas1@st.com

ABSTRACT

Carbon has been co-implanted to phosphorus at low temperature (-100°C) in silicon. As compared to a room temperature carbon implant, phosphorus activation is increased due to the suppression of extended defects. The unusual carbon depleted region observed in both secondary ion mass spectroscopy and atom probe tomography annealed profiles has been explained and modeled using an interstitialcy diffusion barrier of 0.6 eV. Carbon clusters have been interpreted as being composed of several immobile dimers carbon/self-interstitial, in agreement with the stoichiometry of the SiC phase. From the model presented here, an adequate temperature window ($>750^{\circ}\text{C}$) has been found regarding self-interstitials trapping by carbon.

Published under an exclusive license by AIP Publishing. <https://doi.org/10.1063/5.0049782>

I. INTRODUCTION

In the semiconductors industry, amorphizing ion implantations are employed to promote dopant activation during Solid Phase Epitaxy Regrowth (SPER). One well-known advantage is the activation of dopants at concentrations higher than the solubility limit.^{1,2} Another benefit is to achieve activation at temperatures down to 450 and 400 $^{\circ}\text{C}$ in silicon and germanium, respectively.^{3,4}

However, from the SPER completion to the end of annealing, ion implantation induced self-interstitials transiently enhance boron and phosphorus diffusion. Besides the spreading of dopants profiles,^{5,6} Transient Enhanced Diffusion (TED) is also known to induce electrical dopant deactivation through precipitations and segregations at crystalline defects.^{7,8} These issues can still be attenuated, if not suppressed, by using short annealings or carbon co-implantation.^{9,10} In the latter case, carbon acting as a sink for self-interstitials, dopant diffusion, and crystalline defects formation are hindered resulting in improved electrical activations.

Another solution to reduce TED is to increase the initial distance between dopants and generated self-interstitials. This can be done by pushing the Amorphous/Crystalline (A/C) interface deeper in the substrate, for example, with germanium or carbon ion implantation. In a recent study, carbon was co-implanted at

medium energy in silicon to reduce phosphorus diffusion and suppress crystalline defects.¹¹ While phosphorus diffusion was reduced and End-Of-Range (EOR) defects were suppressed, other defects were still formed due to a buried and broad amorphous layer.

In the present study, the objective is to get a deeper understanding of low temperature (-100°C) ion implantation. While the same carbon/phosphorus implant sequence was employed, the wafer was maintained at -100°C during carbon implant with the aim of suppressing crystalline defects and increase phosphorus activation. A focus was done to understand and simulate the carbon depleted region close to the former A/C interface. The model developed hereby helped determine an adequate temperature window for the post-implantation annealing.

II. EXPERIMENT DETAILS

A thin oxide of few nanometers was deposited on a (100) oriented 300 mm silicon wafer. For the sake of confidentiality, the exact energies and doses of ion implantations shall not be mentioned. Therefore, the scale markers along the implantation depth axis are omitted in figures. First, carbon was implanted on a VISta Trident CrionTM in order to reach a maximum concentration close to 10^{20} cm^{-3} at the A/C interface. The wafer was maintained at

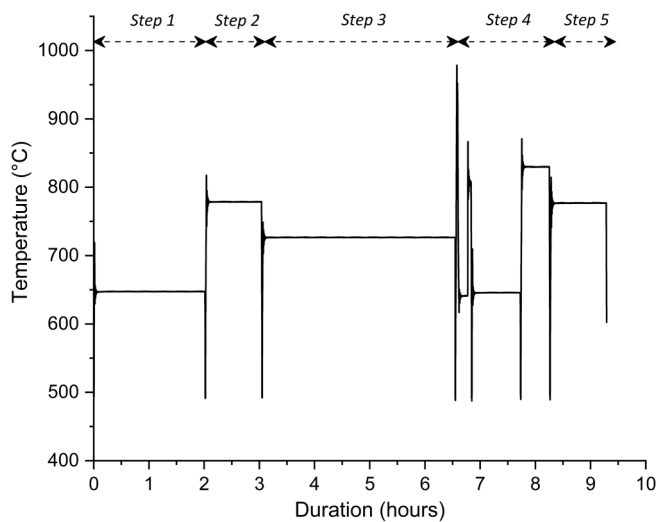


FIG. 1. Annealing sequence performed on carbon/phosphorus implanted silicon.

−100 °C during this implantation. Then, phosphorus was implanted in normal conditions (wafer at 20 °C) at a dose and energy close to 10^{14} cm^{-2} and 100 keV, respectively. To minimize channeling, a tilt of 3° and a twist of 22° were used for all

implantations. A 10-h long annealing sequence composed of five steps was then performed in order to mimic the thermal budget of a real process flow (Fig. 1). Profiles of implanted species were measured after each step by Secondary Ion Mass Spectroscopy (SIMS) using a cesium beam at 4 keV. Amorphization and structural defects were investigated using Transmission Electron Microscopy (TEM) at a 200 kV accelerating voltage. Carbon distribution at the atomic scale was obtained from a Laser-Assisted-Wide-Angle Tomographic Atom Probe¹² (CAMECA-LAWATAP), using short laser pulses (350 fs at 10 nJ/pulse focused on a 0.1 mm spot diameter) at a 343 nm wavelength. A description of the preparation of tips for atom probe tomography analyzes can be found in Ref. 13. Sheet resistances of implanted silicon after annealing were measured from a KLA-TencorTM RS100 system using the four-probe method.

III. TEM/SIMS/APT RESULTS AND QUALITATIVE DISCUSSION

The effect of carbon implant temperature on defects formation is highlighted in Fig. 2. Maintaining the wafer temperature at −100 °C during carbon implant leads to the formation of an amorphous layer that extends up to the surface [Fig. 2(c)]. As a result, the formation of the so-called “zipper” dislocations^{11,14} is prevented. The formation of Microcrystalline Pockets (MPs) and hairpin dislocations¹⁴ is prevented as well because the A/C interface obtained after the implant is steeper. In short, by only decreasing

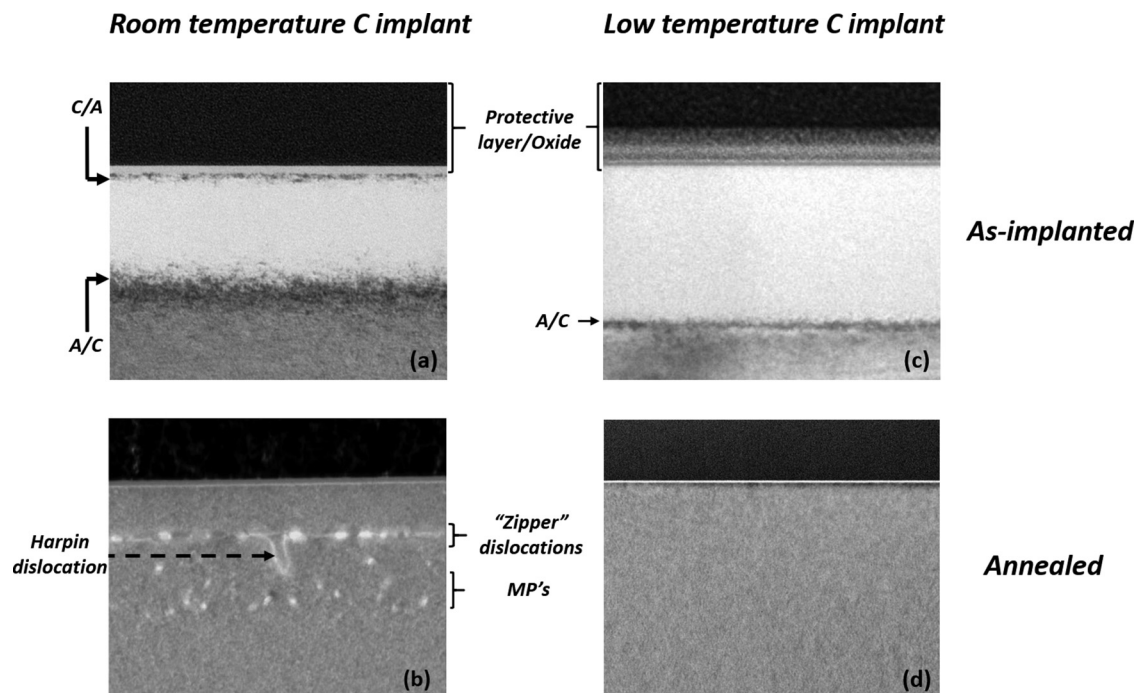


FIG. 2. Cross section TEM images of carbon/phosphorus implanted Si. (a) and (b) are taken from Ref. 11. (c) and (d) are the images related to the low temperature carbon implant. The annealed state was obtained after applying the whole thermal treatment sequence (Fig. 1).

the wafer temperature during carbon implant, no more structural defects, including EOR, are observed after annealing. It is worth mentioning that tiny self-interstitials aggregates (less than 40 interstitials per aggregate) may be small enough not to be resolved by TEM.¹⁵

The effect of the low temperature carbon implant on phosphorus diffusion is revealed in Fig. 3(a). Annealed and as-implanted phosphorus profiles almost overlap. Considering that phosphorus diffusion is interstitially mediated,¹⁶ this indicates that the concentration of self-interstitials remains low upon annealing. The same conclusion was reached using room temperature carbon ion implantation.¹¹ However, in this case, defects still remain after annealing [Fig. 2(b)]. Electrical deactivations may then occur through phosphorus segregations at defects. This is consistent with the fact that a higher sheet resistance has been measured in the room temperature case ($220.1 \pm 0.6 \Omega/\text{sq}$) as compared to the low temperature one ($214.5.1 \pm 0.6 \Omega/\text{sq}$). Hence, we conclude that the absence of extended defects goes along with increased phosphorus activation.

Carbon diffusion is assisted by self-interstitials as well,

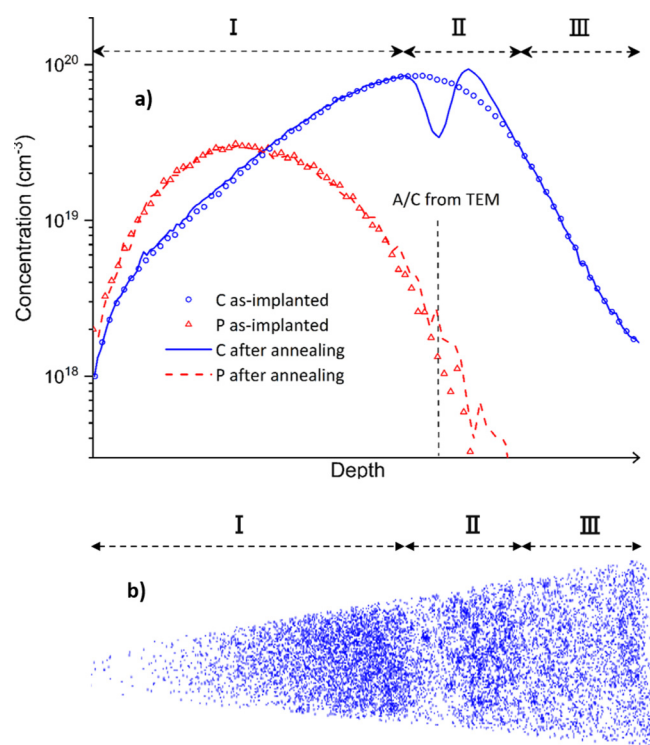
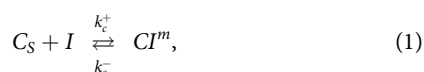


FIG. 3. (a) SIMS profiles of carbon/phosphorus implanted Si (b) APT map of the distribution of carbon atoms after annealing. The annealed state was obtained after applying the whole thermal treatment sequence.

where C_S denotes an immobile substitutional carbon, I is a free self-interstitial, and CI^m is a mobile dimer (sometimes called dumbbell) composed of one silicon atom and one carbon atom sharing the same lattice site.¹⁷ Such a dimer was experimentally identified by Watkins and Brower.¹⁸ Note that reaction (1) is consistent with the so-called “interstitialcy” mechanism. k_c^+ is defined as the capture rate (s^{-1}) of self-interstitials by substitutional carbons and k_c^- the dissociation rate (s^{-1}) of dimers.

During SPER of amorphous layers, carbon atoms are put into substitutional sites if implanted concentrations do not exceed $3.0\text{--}7.0 \times 10^{20} \text{ cm}^{-3}$.¹⁹ Above these values, the strain effect induced by the size difference between carbon and silicon atoms is such that defects are introduced. Since as-implanted concentrations (Fig. 3) are below this range and that no defects have been reported (Fig. 2), we conclude that the carbon dose initially present in amorphous silicon becomes substitutional just after SPER. However, this substitutional amount is metastable since it is well above the solubility limit of carbon in silicon ($\sim 10^{15} \text{ cm}^{-3}$ at 1000°C).²⁰ Thus, a decrease in the substitutional content is expected upon annealing through reaction (1). However, no sign of diffusion/precipitation is evidenced for the most part of recrystallized Si (region I in Fig. 3). This means that a low self-interstitial concentration is maintained in recrystallized silicon all along annealing.

A pronounced carbon depleted region is evidenced close to the former A/C interface (region II). This indicates that both concentrations of self-interstitials and substitutional carbon are high enough to drive diffusion [reaction (1)]. Region II makes indeed the transition between a region rich in C_S 's but poor in I 's (region I) and a region poor in C_S 's but rich in I 's (region III) due to the presence of implant induced self-interstitials. Note, however, that this diffusion is rather unusual because of its asymmetry. Indeed, everything happens as if carbon atoms moved unidirectionally toward the bulk. Furthermore, this diffusion is interrupted rather quickly as evidenced by the carbon bump at the end of II.

No more sign of diffusion is visible after the carbon bump, where Si remained fully crystalline after ion implantation. Indeed, while this region is rich in self-interstitials during TED, it is poor in substitutional carbon since no recrystallization occurred. Our interpretation is that the carbon content in region III is already in the form of stable self-interstitials/carbon dimers before annealing.

APT provides three-dimension maps featuring atom distribution. The 3D distribution map of carbon atoms after annealing, in which each dot represents one atom, is represented in Fig. 3(b). The homogeneous distribution of atoms in recrystallized Si (region I) attests to the presence of substitutional carbon. The depleted region is clearly evidenced just after the end of recrystallized Si. Clusters are found in region II, especially close to the bump region of the SIMS profile. The carbon content in these clusters was recently found to be close to the stoichiometry of the SiC phase present in the phase diagram.¹³ Other studies confirm this result.^{21,22} It is worth mentioning that these clusters are found below the former A/C interface, in the self-interstitial enriched region. Hence, our interpretation is that carbon clusters are composed of several immobile dimers, each immobile dimer resulting from the interaction between a mobile dimer CI^m and a self-interstitial aggregate. Note that this interpretation is consistent with clusters having the same stoichiometry as the SiC phase.

IV. DESCRIPTION OF THE MODEL

A one-dimensional spatial and temporal model accounting for carbon diffusion after amorphizing implants is presented in the following. The ambition is to predict the depleted region observed in Fig. 3 and to determine an adequate temperature window for the post-implantation annealing. Hereafter, $S_I = \frac{[I]}{[I]^+}$ denotes the self-interstitials supersaturation where $[I]$ and $[I]^+$, respectively, represent the concentration of self-interstitials and the one at equilibrium.

A. Self-interstitials aggregates

Every reaction, equation, and assumption presented in this section was taken from preexisting models simulating TED.^{15,23,24} Self-interstitials exchanges between aggregates of adjacent sizes is represented in Fig. 4. I_n denotes a self-interstitial aggregate composed on n self-interstitials ($n > 2$). k_n^+ and k_n^- are the capture rate of I 's by I_n 's (s^{-1}) and the emission rate of I 's by I_n 's (s^{-1}), respectively (Fig. 4). Hence, at a given temperature T and depth x ,

$$\frac{d[I_n]}{dt} = k_{n-1}^+[I_{n-1}]S_I - k_n^+[I_n]S_I - k_n^-[I_n] + k_{n+1}^-[I_{n+1}], \quad (2)$$

$$k_n^+ = 4\pi a_c^n D_I [I^+], \quad (3)$$

$$k_{n+1}^- = k_n^+ \exp\left(\frac{E_f^{n+1}}{k_B T}\right). \quad (4)$$

Equation (4) is taken from Ortiz *et al.*²³ assuming that capture and emission rates of self-interstitials are equal at equilibrium. a_c^n is the capture radius of defects of size n and k_B is the Boltzmann constant. E_f^{n+1} is by definition the energetic cost to add one self-interstitial to one aggregate of size n . It will be termed hereafter the formation energy. $D_I[I^+]$ is assumed to follow an Arrhenius law of prefactor $1.59 \times 10^{25} \text{ cm}^{-1}/\text{s}$ and the activation energy of 4.702 eV.²⁵

For small defects sizes ($n < 10$ in this study), I_n 's are considered to be spherical. In this case, the capture radius is equal to the geometrical one. This leads to $a_c^n = \frac{3n\Omega}{4\pi}^{1/3}$, where Ω is the volume occupied by a silicon atom in the diamond structure (20.02 \AA^3). For this range, E_f^n was deduced experimentally by Cowern *et al.*²⁴

For bigger aggregate sizes ($n \geq 10$ in this study), a rectangular shape is considered. These defects composed of $\langle 110 \rangle$ rows of self-interstitials are assumed to have a constant width (4 nm) and density ($5 \times 10^{14} \text{ cm}^{-2}$). In this context, the length of these defects

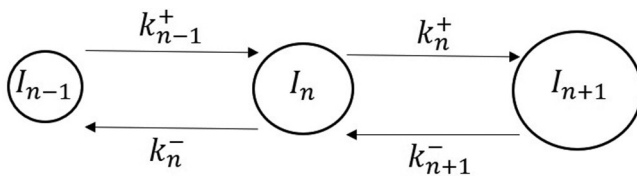


FIG. 4. Growth and dissolution of self-interstitials aggregates of adjacent sizes.

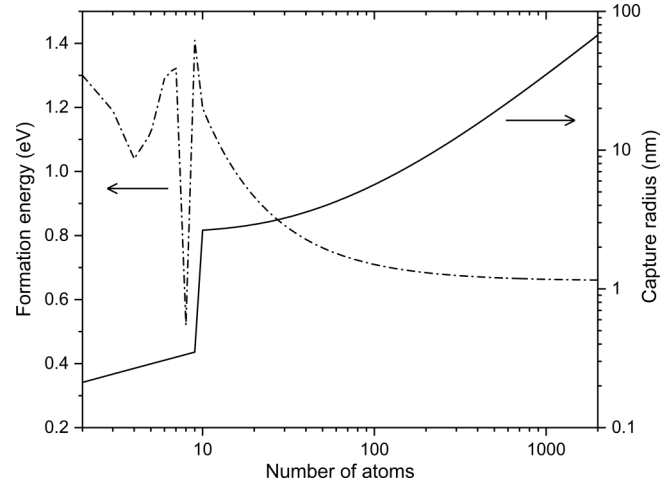


FIG. 5. Formation energy and capture radius of self-interstitials agglomerates.

is simply proportional to n . Details of the capture radius calculation are given in Ortiz *et al.*²³ As for the formation energy, it relies on the strain energy of $\{113\}$ defects which is defined as the energy of two edge plus two mixed dislocations.²³

The formation energy and the capture radius are plotted in Fig. 5. Note the abrupt transition in formation energy between $n = 8$ and $n = 9$ that forces initially the growth of very small defects. Once some lucky defects surpass the I_9 barrier, their ripening in bigger defects is promoted since a_c^n (respectively, E_f^n) monotonically increases (respectively, decreases) with ascending n .

B. Carbon diffusion and clustering

Carbon diffusion is usually illustrated as follows: a fast-migrating dimer CI^m is formed from reaction (1) performs a “long-hop” before returning to the substitutional position. The mean projected path length travelled by migrating dimers increases for decreasing temperatures ($\sim 20 \text{ nm}$ at 850°C , Ref. 26), hence reflecting the increasing difficulty for dimers to return to substitutional sites at lower temperatures.

Hence, due to the high concentration of self-interstitials in region II (Fig. 3), carbon is expected to diffuse out equally in regions I and III. However, no diffusion is observed from region II to III. Everything seems to happen as if there were barriers preventing dimers to flow in recrystallized Si. Since recrystallized Si is rich in substitutional carbon, the following reaction would occur: $CI^m + C_S \leftrightarrow CI^m C_S$, where $CI^m C_S$ is an immobile complex composed of two carbon atoms and one silicon atom. However, since these complexes are unstable at annealing temperatures,^{17,27} we will assume that they dissociate immediately after formation.

As interpreted in part III, we assume hereafter that clusters are composed of several immobile self-interstitial/carbon dimers. For the modeling part, a mobile dimer is first formed from reaction (1), migrates until it interacts with a self-interstitial aggregate, and, therefore, becomes immobile: $CI^m + I_n \rightarrow CI^I + I_n$. Considering the two previously defined reactions and assuming that they are

diffusion-limited, the mean macroscopic projected length travelled by dimers prior to reacting either with a substitutional carbon or an aggregate is given by

$$L_T = \frac{1}{\sqrt{2\pi} (a_{C_S}[C_S] + \sum_{n=2}^{n_{max}} a_{I_n}[I_n])}, \quad (5)$$

where a_{C_S} is the capture radius of dimers at substitutional carbon atoms. An order of magnitude of L_T is given as follows. Taking $a_{C_S} = a_{I_2}$ and $[C_S] = [I_2] = 10^{19} \text{ cm}^{-3}$ gives $L_T \sim 6 \text{ nm}$. This is three times smaller than the long-hop distance traveled by dimers before returning to the substitutional position at 850°C ($\sim 20 \text{ nm}$).²⁶ Furthermore, the concentrations of C_S and I_n should be, at least initially, higher than those given in this example, and the temperatures smaller than 850°C (Fig. 1). In other words, dimers never return in the substitutional position because L_T is smaller than the long-hop distance. The substitutional content being decreased, this view is consistent with a progressive return to equilibrium (part III).

Carbon diffusion modeling is sum up as follows. As long as a mobile dimer CI^m does not interact with a self-interstitial aggregate, it performs “stop and go” events at substitutional carbon atoms in agreement with the work of Mattoni *et al.*¹⁷ Three carbon configurations are considered: immobile C_S , mobile CI^m , and immobile CI^i . The dissociation reaction $CI^m \rightarrow C_S + I$ never occurs so that the concentration of substitutional carbon at a given depth x reads

$$\frac{d[C_S]}{dt} = -k_C^+[C_S]S_I, \quad (6)$$

$$k_C^+ = 4\pi a_{ko} D_I [I^*] \exp\left(-\frac{E_C^+}{k_B T}\right), \quad (7)$$

where a_{ko} is a capture radius (0.27 nm in this model) and E_C^+ is the energy barrier to reaction $C_S + I \rightarrow CI^m$.

C. Self-interstitial supersaturation and role of the surface

The self-interstitial supersaturation S_I relies on reactions (2) and (6). At a given depth x , S_I reads

$$\frac{dS_I}{dt} = \frac{1}{[I^*]} \left\{ D_I [I^*] \frac{d^2 S_I}{dx^2} - 2k_1^+[I^*]S_I^2 + 2k_2^-[I_2] - k_C^+[C_S]S_I - \sum_{n=2}^{N_{max}} (k_n^+[I_n]S_I - k_{n+1}^-[I_{n+1}]) \right\}. \quad (8)$$

Note the negative contribution of substitutional carbon: consumed self-interstitials are not released back because the reaction $CI^m \rightarrow C_S + I$ never occurs. This equation includes Fick's second law term as well. Factor 2 indicates that two I s are captured (respectively, emitted) through $I + I \rightarrow I_2$ (respectively, $I_2 \rightarrow I + I$) reactions. N_{max} is the maximum size n of self-interstitials aggregates I_n ($N_{max} = 2000$).

The surface is here considered as a perfect sink for self-interstitials. However, its effect is thought to be negligible since the distance between the defects and the surface is large ($>100 \text{ nm}$).¹⁵

V. VALIDITY OF THE MODEL AND QUANTITATIVE DISCUSSION

A. Initial concentrations

In non-recrystallized Si (II and III in Fig. 3), initial self-interstitials concentrations have been estimated from the “excess interstitials model” (Ref. 15): $[I_{ex}] = [I_0] - [V_0] + [A_S]$, where I_0 and V_0 denote the self-interstitials and vacancies induced by ion implantation in crystalline silicon and A_S is the self-interstitials induced by dopant activation ($P_I \rightarrow P_S + I$). Here, the incorporation of carbon atoms in substitutional sites should also be considered. However, we assumed that carbon atoms present in crystalline Si before annealing are initially in the form of immobile dimer CI^i . Furthermore, the phosphorus dose implanted in crystalline silicon is negligible ($\sim 1\%$ of the total dose) and so is the generation of self-interstitials. As a result, $[A_S] = 0$.

I_0 and V_0 have been obtained from a KMC simulator.²⁵ We further assume that the induced self-interstitials are gathered in the form of dimer I_2 before annealing (Fig. 6). For the sake of simplicity, we did not consider diffusion in amorphous silicon so that our simulation begins from an already recrystallized Si. However, we checked from SIMS profiles that no impurities redistribution occurred during SPER. Therefore, the initial carbon concentrations have been simply derived from the as-implanted profile (Fig. 3) and the amorphous volume fraction $f_{amo}(x)$ obtained from the KMC simulator. At a given depth x , $f_{amo} = 1$ (respectively, 0) when all sub-volumes are amorphous (respectively, crystalline). Thus, $f_{amo}(x)C_{imp}(x)$ gives the concentration of carbon atoms in amorphous silicon at a depth x . Similarly, $(1 - f_{amo}(x))C_{imp}(x)$ is the concentration of carbon atoms in crystalline silicon at a depth x . Hence, since our model begins with an already recrystallized silicon, $f_{amo}(x)C_{imp}(x)$ is the substitutional concentration at $t=0 \text{ s}$ at

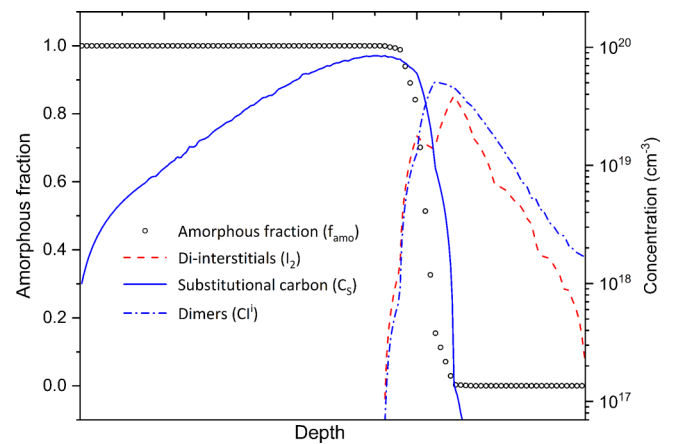


FIG. 6. Initial profiles obtained from as-implanted SIMS (Fig. 3) and the Sentaurus KMC software.²⁵

a depth x . On the other hand, $(1 - f_{amo}(x))C_{imp}(x)$ is the concentration of immobile dimers CI^i at a depth x (Fig. 6).

B. Simulation results

Equations (2), (6), and (8) have been solved using an adaptive Runge–Kutta 4 method. The only two free parameters of the model are a_{Cs} and E_C^+ .

E_C^+ is the most critical one since it monitors the rate at which region II depletes. $E_C^+ = 0.5$ eV is the minimum barrier such as no diffusion occurs during the first annealing step, in agreement with intermediary SIMS profiles (not shown). Finally, $E_C^+ = 0.6$ eV has been found to be the best value to reproduce the final magnitude of the depleted region. On the other hand, simulated profiles are much less sensitive to a_{Cs} . 2 nm has been found to be the optimum capture radius to account for the abruptness of the positive slope region of the depleted region.

Simulated profiles are shown in Fig. 7. The model reproduces very well the position and the shape of the depleted region. Still, the magnitude is somewhat larger, and the enriched zone is centered a bit deeper than that of the SIMS. It is also worth mentioning that the abruptness of the depleted region could not be reproduced without introducing a probability factor for I^i s to flow into region I. This factor is inspired by the work of Aboy *et al.*²⁸ Let us consider a self-interstitial emitted from a given aggregate I_n at the middle of region II + III. This interstitial flows toward an adjacent aggregate in the direction of recrystallized Si with a probability 1/6. Then, the probability for the self-interstitial to flow in region I is defined as the ratio between the mean distance across aggregates and that to reach recrystallized Si,

$$p = \frac{1}{6} \frac{[D_m]^{-1/3}}{[D_m]^{-1/3} + l_{out}}, \quad (9)$$

where $[D_m]$ is the mean concentration of aggregates in regions II and III and l_{out} is half the width of region II + III. This probability factor monitors the proportion of self-interstitials exchanged between aggregates as compared to those flowing into recrystallized Si.

Kinetics of self-interstitials capture by carbon atoms is depicted in Fig. 8. During the first annealing step, the substitutional loss is almost null while the self-interstitials density in aggregates stays almost constant. Since the isotherm temperature shifts from 645 °C for the first annealing step to 775 °C for the second one, a net decrease (respectively, increase) of the self-interstitials density in aggregates (respectively, substitutional loss) occurs. The decreasing (respectively, increasing) rate becomes smaller during the third annealing step as the temperature is lowered. Finally, TED stops during the hot ascending ramp of the fourth annealing step (Fig. 1): every implant induced self-interstitial is consumed. According to this model, 95% of self-interstitials are consumed from the reaction $C_s + I \rightarrow CI^m$. The remaining 5% either diffused into the bulk or recombined at the surface. Hence, the final magnitude of the depleted zone is essentially equal to the initial density of excess self-interstitials ($2.4 \times 10^{14} \text{ cm}^{-2}$) given by the KMC simulator. To sum up, while the energy barrier E_C^+ controls the rate at which region II depletes, the final depletion is governed by the initial density of excess self-interstitials. Another conclusion arising

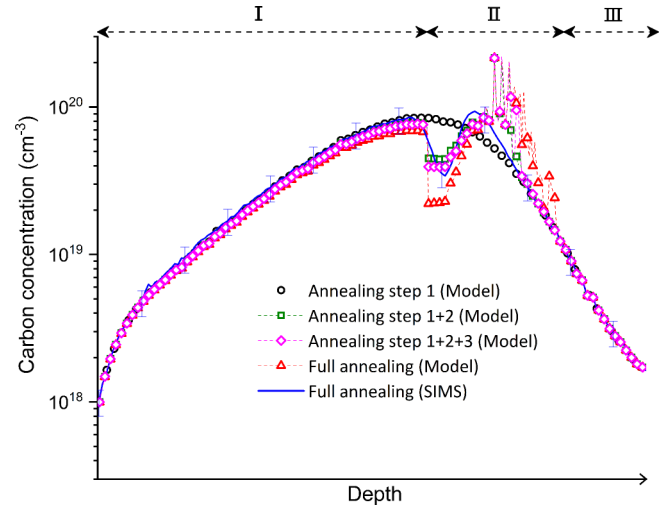


FIG. 7. Simulated carbon profiles at different annealing steps ($E_C^+ = 0.6$ eV and $a_{Cs} = 2$ nm). Error bars delimit the uncertainty related to the SIMS concentration.

from Figs. 7 and 8, is that the annealing temperature should be higher than 750 °C to get a significant capture rate of self-interstitial by carbon.

The transient nature of accelerated diffusion is illustrated in Fig. 9. First note that the abrupt transition between regions I and II + III result from the factor p defined in Eq. (9). S_I tends to 1 when getting closer to the perfect sink at the surface. In region II + III, S_I is well above 1 during the three first annealing steps, indicative of a TED regime. When the annealing temperature reaches 950 °C during the ascending ramp of the fourth annealing

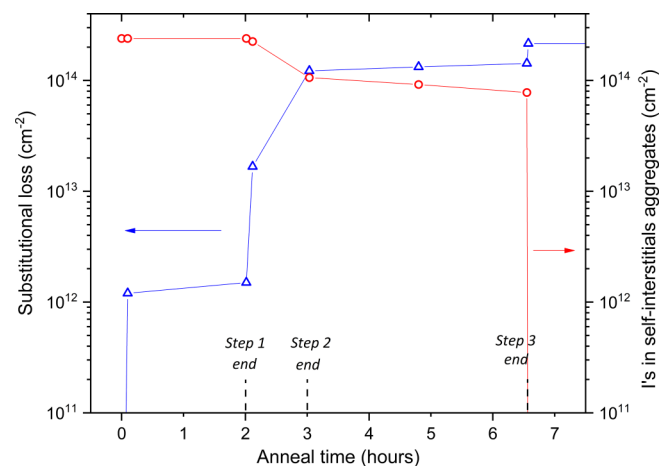


FIG. 8. Substitutional loss (Δ) and I^i s density in self-interstitials aggregates (O) as a function of the annealing time ($E_C^+ = 0.6$ eV and $a_{Cs} = 2$ nm).

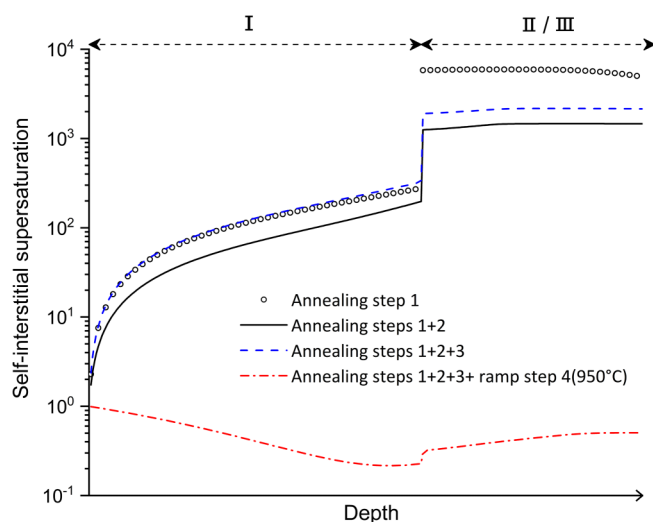


FIG. 9. Self-interstitial supersaturation at different annealing steps ($E_C^+ = 0.6$ eV and $a_{CS} = 2$ nm).

step, every implant induced I is consumed and TED stops. Since almost no reactions $C_S + I \rightarrow CI^m$ occur in recrystallized Si, substitutional concentrations are still well above the solubility limit in region I. The higher the concentration of substitutional carbon, the higher the undersaturation of self-interstitials ($S_I < 1$) in recrystallized Si, in agreement with the work of Scholz *et al.*²⁹

To assess the magnitude of diffusion induced by the rest of the fourth and the fifth annealing step, let us assume as a worst case that the concentration of self-interstitials is constant and not undersaturated ($S_I = 1$). Hence, at a given T , $[C_S]$ follows an exponential law of time constant $\tau = 1/k_C^+$ from Eq. (6). In these conditions, 5 h are needed to get a variation of 10% in $[C_S]$ at 850 °C. Since both the temperature and the remaining anneal time are smaller than these values, we conclude that diffusion is negligible once TED is over.

VI. CONCLUSION

Carbon has been co-implanted to phosphorus at low temperature (−100 °C) in silicon. Compared to a standard room temperature carbon ion implantation, amorphization is enhanced resulting in a defect-free doped layer. As a result, phosphorus activation is increased.

Self-interstitials trapping in the self-interstitials enriched region has been modeled using two basics reactions involving carbon: $C_S + I \rightarrow CI^m$ (interstitialcy diffusion) and $CI^m + I_n \rightarrow CI^i + I_n$ (formation of immobile dimers). Thanks to the model established, we have been able to understand and predict the kinetics of the carbon depleted region after annealing: for temperatures higher than 750 °C, the substitutional content close to the ex-amorphous/crystalline interface progressively decreases until every ion implantation induced self-interstitial is consumed.

DATA AVAILABILITY

The data that support the findings of this study are available within the article.

REFERENCES

- ¹K. Suzuki *et al.*, "Maximum active concentration of ion-implanted phosphorus during solid-phase epitaxial recrystallization," *IEEE Trans. Electron Devices* **54**(8), 1985–1993 (2007).
- ²B. J. Pawlak *et al.*, "Enhanced boron activation in silicon by high ramp-up rate solid phase epitaxial regrowth," *Appl. Phys. Lett.* **86**(10), 101913 (2005).
- ³F. P. Luce *et al.*, "Methodology for thermal budget reduction of SPER down to 450 °C for 3D sequential integration," *Nucl. Instrum. Methods Phys. Res., Sect. B* **370**, 14–18 (2016).
- ⁴J.-H. Park *et al.*, "High performance germanium N⁺/P and P⁺/N junction diodes formed at low temperature (≤ 380 °C) using metal-induced dopant activation," *Appl. Phys. Lett.* **93**(19), 193507 (2008).
- ⁵P. A. Stolk *et al.*, "Physical mechanisms of transient enhanced dopant diffusion in ion-implanted silicon," *J. Appl. Phys.* **81**(9), 6031–6050 (1997).
- ⁶N. Cowern and C. Rafferty, "Enhanced diffusion in silicon processing," *MRS Bull.* **25**(6), 39–44 (2000).
- ⁷D. Blavette and S. Duguay, "Investigation of dopant clustering and segregation to defects in semiconductors using atom probe tomography," *J. Appl. Phys.* **119**(18), 181502 (2016).
- ⁸S. Duguay *et al.*, "Direct imaging of boron segregation to extended defects in silicon," *Appl. Phys. Lett.* **97**(24), 242104 (2010).
- ⁹A. Jain, "The reduction of TED in ion implanted silicon," *AIP Conf. Proc.* **1066**(1), 19 (2008).
- ¹⁰P. A. Stolk *et al.*, "Carbon incorporation in silicon for suppressing interstitial-enhanced boron diffusion," *Appl. Phys. Lett.* **66**(11), 1370–1372 (1995).
- ¹¹P. Dumas *et al.*, "3D atomic-scale investigation of carbon segregation in phosphorus co-implanted silicon," *Appl. Phys. Lett.* **115**(13), 132103 (2019).
- ¹²B. Deconihout, F. Vurpillot, B. Gault, G. Da Costa, M. Bouet, A. Bostel, and M. Brunel, "Toward a laser assisted wide-angle tomographic atom-probe," *Surf. Interface Anal.* **39**(2–3), 278–282 (2007).
- ¹³P. Dumas *et al.*, "Atom probe tomography quantification of carbon in silicon," *Ultramicroscopy* **220**, 113153 (2020).
- ¹⁴K. S. Jones, S. Prussin, and E. R. Weber, "A systematic analysis of defects in ion-implanted silicon," *Appl. Phys. A: Solids Surf.* **45**(1), 1–34 (1988).
- ¹⁵A. Claverie *et al.*, "Extended defects in shallow implants," *Appl. Phys. A: Mater. Sci. Process.* **76**(7), 1025–1033 (2003).
- ¹⁶J. S. Christensen *et al.*, "Phosphorus and boron diffusion in silicon under equilibrium conditions," *Appl. Phys. Lett.* **82**(14), 2254–2256 (2003).
- ¹⁷A. Mattoni, F. Bernardini, and L. Colombo, "Self-interstitial trapping by carbon complexes in crystalline silicon," *Phys. Rev. B* **66**(19), 195214 (2002).
- ¹⁸G. D. Watkins and K. L. Brower, "EPR observation of the isolated interstitial carbon atom in silicon," *Phys. Rev. Lett.* **36**(22), 1329 (1976).
- ¹⁹J. W. Strane *et al.*, "Carbon incorporation into Si at high concentrations by ion implantation and solid phase epitaxy," *J. Appl. Phys.* **79**(2), 637–646 (1996).
- ²⁰U. Goesele *et al.*, "Diffusion engineering by carbon in silicon," *MRS Online Proc. Library Archive* **610**, 711 (2000).
- ²¹F. Cristiano *et al.*, "Interstitial trapping efficiency of C+ implanted into preamorphised silicon—Control of EOR defects," *Nucl. Instrum. Methods Phys. Res., Sect. B* **127–128**, 22–26 (1997).
- ²²A. Cacciato *et al.*, "Dislocation formation and B transient diffusion in C coimplanted Si," *J. Appl. Phys.* **79**(5), 2314–2325 (1996).
- ²³C. J. Ortiz *et al.*, "A physically based model for the spatial and temporal evolution of self-interstitial agglomerates in ion-implanted silicon," *J. Appl. Phys.* **96**(9), 4866–4877 (2004).

²⁴N. E. B. Cowern *et al.*, “Energetics of self-interstitial clusters in Si,” *Phys. Rev. Lett.* **82**(22), 4460 (1999).

²⁵Sentaurus Process User Guide (Synopsys Inc., 2019).

²⁶N. Cowern *et al.*, “Diffusion suppression in silicon by substitutional C doping,” in *32nd European Solid-State Device Research Conference* (IEEE, New York, 2002).

²⁷R. Pinacho *et al.*, “Carbon in silicon: Modeling of diffusion and clustering mechanisms,” *J. Appl. Phys.* **92**(3), 1582–1587 (2002).

²⁸M. Aboy *et al.*, “Atomistic analysis of defect evolution and transient enhanced diffusion in silicon,” *J. Appl. Phys.* **94**(2), 1013–1018 (2003).

²⁹R. Scholz *et al.*, “Carbon-induced undersaturation of silicon self-interstitials,” *Appl. Phys. Lett.* **72**(2), 200–202 (1998).